Laser-Driven Shock Acceleration of Ion Beams from Spherical Mass-Limited Targets

A. Henig,[1,2,*] D. Kiefer,[1,2] M. Geissler,[1,3] S. G. Rykovanov,[1,4] R. Ramis,[5] R. Hörlein,[1,2] J. Osterhoff,[1] Zs. Major,[1,2] L. Veisz,[1] S. Karsch,[1] F. Krausz,[1,2] D. Habs,[1,2] and J. Schreiber[1,2,6]

[1]*Max-Planck-Institut für Quantenoptik, Garching, Germany*
[2]*Department für Physik, Ludwig-Maximilians-Universität München, Garching, Germany*
[3]*Department of Physics and Astronomy, Queen's University Belfast, Belfast BT7 1NN, United Kingdom*
[4]*Moscow Physics Engineering Institute, Kashirskoe shosse 31, Moscow, Russia*
[5]*ETSI Aeronáuticos, Universidad Politécnica de Madrid, Spain*
[6]*Blackett Laboratory, Imperial College, London SW7 2AZ, United Kingdom*

(Received 13 September 2008; published 4 March 2009)

We report on experimental studies of ion acceleration from spherical targets of diameter 15 μm irradiated by ultraintense (1×10^{20} W/cm^2) pulses from a 20-TW Ti:sapphire laser system. A highly directed proton beam with plateau-shaped spectrum extending to energies up to 8 MeV is observed in the laser propagation direction. This beam arises from acceleration in a converging shock launched by the laser, which is confirmed by 3-dimensional particle-in-cell simulations. The temporal evolution of the shock-front curvature shows excellent agreement with a two-dimensional radiation pressure model.

DOI: 10.1103/PhysRevLett.102.095002 PACS numbers: 52.38.Kd, 41.75.Jv, 52.50.Jm, 52.65.Rr

Ion acceleration with highly intense laser pulses has been extensively studied over the past years. When thin foils were used as a target, target normal sheath acceleration (TNSA [1]) was found to be the predominant mechanism responsible for the emission of multi-MeV, high-quality ion beams. Relativistic electrons are driven through the target by the intense laser pulse and set up an electric field at the nonirradiated side of the target. Reaching magnitudes above 1 TV/m, those fields ionize atoms in the surface layers and subsequently accelerate the ions, predominantly protons due to their high charge-to-mass ratio, to energies of up to 60 MeV [2] in a collimated beam. The maximum energies obtained under various experimental conditions are well understood [2–4]. Lower energetic protons are produced in the outer regions of the electric field, which extends transversely to a diameter of several 100 μm [5–7]. This enormous lateral extension is attributed to recirculating electrons which spread around the target, thus causing a decay of the acceleration field. Therefore, mass-limited targets, i.e., targets with transverse dimensions comparable to the laser focus are expected to enhance the electric fields, owing to the confinement of recirculating hot electrons, which ultimately results in increased ion energies [8]. With this respect, recent particle-in-cell (PIC) simulations [9,10] and experiments [11,12] favor a spherical target geometry with the drawback of a nearly isotropic ion emission. In this Letter we report for the first time on strongly directed ion beam emission from laser irradiated mass-limited plastic spheres. The protons exhibit a broad spectrum with cutoff energies of up to 8 MeV, which compares to 1–3 MeV obtained from extended aluminum and plastic foils when irradiated under identical laser conditions. Three-dimensional PIC simulations support our interpretation that the directed ion beams are accelerated in a converging shock launched by the laser.

The experiments were conducted using the upgraded ATLAS Ti:sapphire laser at the Max-Planck-Institute for Quantum Optics in Garching. The system delivers light pulses to the target containing 0.6 J of energy within a pulse duration of 45 fs at a center wavelength of $\lambda_0 = 790$ nm. A 15 cm focal length parabolic mirror tightly focuses the 7 cm diameter beam to a measured typical spot size of 3.3 μm full width at half maximum (FWHM) diameter. This yields a peak intensity of around 1×10^{20} W/cm^2, which is equivalent to a dimensionless laser field amplitude of $a_0 \simeq 6.7$. The Strehl ratio, i.e., the ratio of the peak intensity of the measured point spread function (PSF) to the peak intensity of a diffraction-limited PSF of a flattop beam, calculates to 0.29. The relative intensity of both the ASE pedestal and short prepulses on the ps time scale was characterized by a 3rd order autocorrelation measurement, giving a contrast of better than 10^8 (until 4 ps before the main peak). At above 400 ps before the arrival of the main peak, a fast Pockels cell further suppresses the ASE pedestal and prepulses by additional 2 orders of magnitude. A schematic setup of the experiment comprising the frequency-doubled probe beam and the ion detector is shown in Fig. 1(a). The targets were positioned by imaging the focal spot volume with a magnification of around 50 onto CCD cameras. Figure 1(b) shows an exemplary picture of a mass-limited target, i.e., a poly(methyl methacrylate) (PMMA) sphere of 15 μm in diameter mounted on a sub-μm thin glass capillary, as it appears on one of the cameras. The same CCD imaging system was used to capture a snapshot of the sphere right at the time of the interaction using a frequency-doubled transverse probe pulse with a duration of approximately 100 fs as a back-

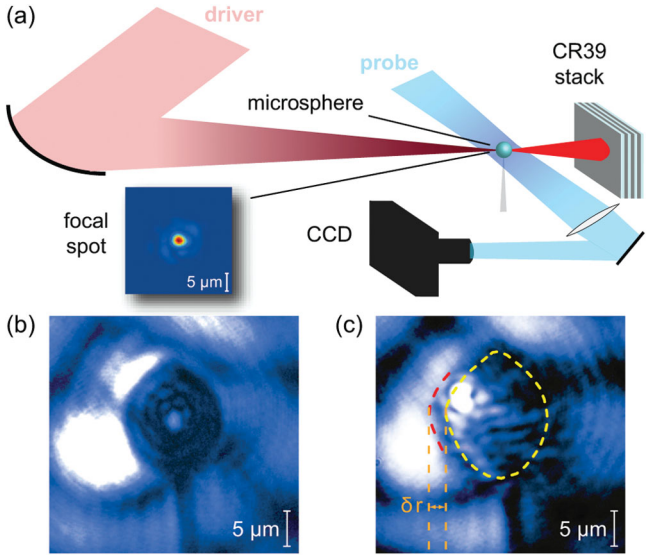

FIG. 1 (color). Experimental setup including a characteristic focal spot image (a) and a picture of a typical microsphere target before the shot (b) and at the time of interaction (c). The white regions visible both in (b) and (c) outside the contour of the spherical target arise from inhomogeneities of the probe beam profile, whereas the bright white spot that appears on the target shadow in (c) is generated by self-emission of the target at the second harmonic of the incident pulse. The increased radius of the sphere δr results from the deflection of the probe-laser pulse in the preformed plasma.

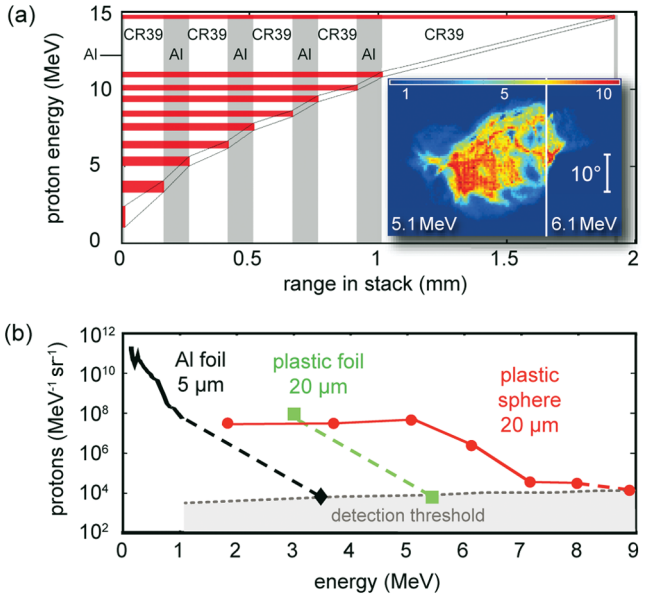

FIG. 2 (color). Proton energies accessible with the applied CR39 stacks (a) and a typical proton beam profile at the highest energy (inset, color bar indicates number of particles in units of $10^6/\mathrm{rad}^2$, energies represent the center of the respective interval). The fine grid structure is an artifact resulting from double counts in the automated scanning analysis. (b) Proton energy distributions from aluminum foils (black), plastic foils (green), and plastic spheres (red). The curves for the plastic targets are extracted from the CR39 stack to appear as in the case of a spectrometer with small angular acceptance (10^{-7} sr) placed in laser propagation direction. The dashed lines are a linear extension of the spectra to the next higher energy level in the stack where no proton signal was observed.

lighter [Fig. 1(c)]. In the image obtained during the interaction the spheres appear about 4.4 ± 0.4 μm larger in diameter, which we attribute to the presence of a preplasma caused by the amplified spontaneous emission (ASE) pedestal. Assuming an exponential density profile and performing ray-tracing calculations for our imaging system ($f/2$), the apparent radial increase of the sphere δr equals twice the distance between the critical surface and the surface of the undisturbed sphere. Thus, we obtain the scale length $l_s = \delta r(2\ln(n_0/n_{c,\lambda_0/2}))^{-1} \simeq 0.3$ μm where n_0 is the electron density of a fully ionized PMMA sphere and $n_{c,\lambda_0/2}$ is the critical density for the probe-laser pulse. This value is in excellent agreement with one-dimensional calculations for our prepulse conditions that were done using the hydrodynamic code MULTI [13]. Besides displaying the shadow of the expanded preplasma, Fig. 1(c) also shows the self-emission of the target at the second harmonic of the incident pulse, giving a measure of the laser focal spot size and position on the target surface. Stacks of CR39 plastic track detectors alternating with aluminum foils were used to record the proton beam profile at different energies. Figure 2(a) shows the sensitivity in energy of a typical stack used in our experiments. After irradiation, the CR39 plates were etched in sodium hydroxide to make each ion impact visible, so that the absolute number of accelerated ions could be counted with an automated scanning microscope. Unmistakable identification of protons is enabled by their characteristic damage spots imprinted in CR39. Only protons which are stopped close to the front or the rear surface of the CR39 plates are visible, which allows the definition of a detectable energy interval for both sides of each layer of the stack. The energy losses of protons inside the detector stack were calculated using the stopping power data tabulated in the SRIM package [14]. In order to reduce the gaps in energy between intervals, the stack was split by using an additional 50 μm aluminum filter covering one half of the area. Alternatively, the detector stack could be replaced by a Thomson parabola spectrometer which was used for the measurement of ions accelerated from aluminum foil targets. Although Thomson parabola spectrometers are frequently used to detect ions accelerated by high intensity laser pulses, their main drawback is the small acceptance angle which is usually less than 1 μsr, resulting from a pinhole of around 100 μm in diameter placed at a distance of up to 1 m. In the experiments presented here, the detector stack covered a solid angle of $\sim$0.5 sr (i.e., $\sim \pm 20°$) in forward direction.

A typical profile of the proton beam produced from a mass-limited target is shown in the inset of Fig. 2(a). The images are obtained by counting the ion impacts on each

CR39 plate and plotting a two-dimensional histogram. In fact, the resulting figures show the same information as may be obtained by a two-dimensional detector with a linear response on the number of incident ions. For smaller energies, similar proton profiles with comparable angular divergences of 30–40° are obtained except for the lowest energy of around 1 MeV. Here, the CR39 plates were homogeneously irradiated which we attribute to an isotropically emitted proton beam. Owing to the small spatial separation of ion impacts on the low energy layers of the stack, the automated scanning system could not be used. Therefore, we manually counted representative parts of the CR39 plates which allows us to obtain the spectral distribution as it would appear in a spectrometer with a small angular acceptance ($\sim \mu$sr). The proton spectrum obtained for the spheres is compared with results from irradiated foils in Fig. 2(b). For 5 μm thick aluminum foils the exponential spectrum usually extends to energies between 1 and 2 MeV (black solid line), while we observed 3 MeV protons from a 20 μm thick plastic foil (green). The flat spectrum of the protons accelerated from the spheres extends to 8 MeV. It is noteworthy, that an energetic, highly directed proton beam originating from the irradiation of a microsphere was seen in approximately one out of four shots. We attribute this limit in reproducibility to a random pointing instability of the laser focus on target of $\sim \pm 5$ μm. A more detailed discussion will follow later in the text.

Evidently, spherical targets emit proton beams into an angle of divergence comparable to that observed for extended foils. This observation contradicts the assumption that ions are predominantly emitted from the surfaces of the sphere, where a nearly isotropic emission pattern is expected. To explain this behavior, we conducted three-dimensional particle-in-cell simulations using the code ILLUMINATION [15]. The experimental setup was modeled by placing a sphere of diameter 6.4 μm at the center of a rectangular simulation box with dimensions 23 μm in transverse and 54 μm in longitudinal, i.e., laser propagation direction, which is smaller than the actual sphere size of around 15–20 μm owing to computational limitations. The microsphere was composed of a preionized hydrogen plasma with an initial electron density of 10^{22} electrons/cm^3. To remove the influence of unwanted reflections, absorbing layers were added to the boundaries of the box. We chose 46 and 23 nm as transverse and longitudinal grid size, respectively. The laser pulse was of hyperbolic secant envelope shape with parameters such as FWHM pulse duration, spectrum center wavelength, Gaussian focal spot FWHM diameter at the center of the simulation box, and dimensionless laser field amplitude chosen to match the actual experimental settings.

Although the real density of the targets is considerably higher than the microsphere density used in the simulations, the laser-plasma interaction is expected to happen within the preplasma at density values around the relativistically corrected critical density γn_c, where $\gamma = (1 + a_0^2/2)^{1/2}$ and $n_c = 1.75 \times 10^{21}$ electrons/cm^3 which for our parameters gives 8.5×10^{21} electrons/cm^3. The presence of a preplasma is expected for our prepulse conditions and was observed in the images of the spheres obtained within the time window of the interaction [Fig. 1(c)]. Figure 3(a) shows the ion-density distribution in the plane of laser polarization obtained from the 3D-PIC simulations and every 8th proton (macroparticle) close to this plane with energies above 1 MeV. The snapshot was taken 133 fs after the interaction of the laser pulse maximum with the sphere. It is apparent from this picture that the directed ion beam originates from the interaction zone (red dots) where a converging shock structure forms. In fact, closer analysis reveals that the fastest ions move with twice the shock velocity as expected for shock acceleration [16]. The ions from the surface of the sphere (yellow dots) are emitted almost isotropically into 4π, which was reported in a number of recent studies using PIC codes [8–10,17] and is confirmed experimentally [11,12]. This behavior is contrary to the case of a flat foil irradiated under identical conditions [Fig. 3(b)]. The TNSA ions are now directed, while the shock established at the target front is divergent, owing to the laser hole-boring which also reflects in a larger divergence of the accelerated proton beam. For a better understanding of the directed emission we adapt the formula for the shock-velocity $v_s/c = a_L/\sqrt{2}\,(m_e/m_i)^{1/2}(n_c/n_i)^{1/2}$ [18], where m_i and m_e are ion and electron mass, n_i and n_c are ion density and critical density for the driving laser pulse. The laser amplitude $a_L = a_0 f(r)$ varies with the radial coordinate r with a Gaussian shape according to our simulations, i.e., $f(r) = \exp(-2\ln 2\, r^2/w^2)$ where w is the FWHM diameter of the spatial intensity distribution. Depending on the local angle

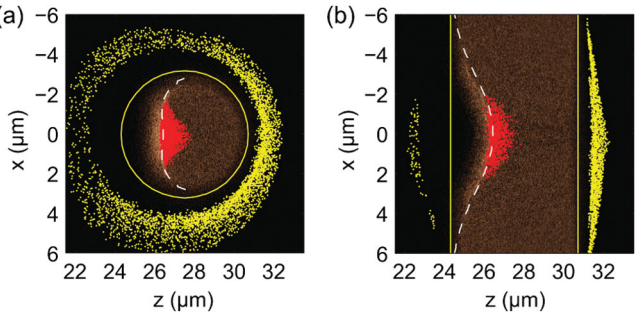

FIG. 3 (color). Color-scale plot of the proton density (ranging from 0 to 4×10^{22}/cm^3) obtained from 3D-PIC simulations 133 fs after the arrival of the laser pulse maximum on a sphere (a) and a foil (b) target. The yellow lines indicate the initial target boundaries. Protons with energy in access of 1 MeV are represented by yellow and red dots, marking surface and shock accelerated ions, respectively. The white dashed lines illustrate the shock front as calculated using the analytical model which is described in the text.

of incidence α, the intensity must be corrected by multiplication with $\cos\alpha$. The direction of the radially varying shock velocity with magnitude $v_m = v_s(\cos\alpha)^{1/2}$ is given by the gradient of the reflecting surface $z(r)$, i.e., the shock front. Using $\tan\alpha(r,t) = \partial z/\partial r|_{(r,t)}$, we obtain the equations of motion for the points defining the shock front

$$\frac{dr}{dt} = v_r(r,t) = -v_s \partial z/\partial r[1 + (\partial z/\partial r)^2]^{-3/4},$$
$$\frac{dz}{dt} = v_z(r,t) = v_s[1 + (\partial z/\partial r)^2]^{-3/4}, \quad (1)$$

which can be integrated numerically over the laser pulse duration τ_L. For the sake of simplicity, we assumed the pulse envelope to be flattop in time. The shape of the shock front at later times is then obtained by propagating each point (r, z) using the corresponding velocity $(v_r(\tau_L), v_z(\tau_L))$. The result of this simple consideration is depicted by the white dashed lines in Figs. 3(a) and 3(b) for the two initial geometries. Given the simplicity of our assumptions, the agreement of those estimates with the 3D-PIC results is quite remarkable. Calculations of the shock front for 15–20 μm diameter spheres closely resemble the results obtained for 6.4 μm, which validates the applicability of our PIC simulations to model the experimental observations. Introducing a transverse offset of 5 μm in the position of the laser focus, corresponding to the experimentally observed random pointing fluctuations of the incident beam on target, leads to a deflection of the shock-front propagation direction of $\sim 30°$ for a 20 μm diameter sphere, as well as a slight reduction in proton energy. Such a large deviation would exceed the detector acceptance half angle of 20°, causing the shock accelerated proton beam to miss the CR39 stack. Based on these considerations, we attribute the experimentally observed limit in reproducibility to the known jitter in the pointing of the laser focus.

Finally, we compared the angular distributions of protons obtained from the PIC simulations for a foil and a sphere target, dividing each into components accelerated from the front and from the rear surface, respectively. Motivated by the observation of the shock front, only protons with velocities greater than the shock velocity in the center were considered (energies above 1 MeV). For the foil target, the flux of the ions emitted from the rear surface exceeds the one of the front accelerated ions by a factor of 10. In the case of the sphere the result is inverted, the proton beam from the front is about 50 times as intense as the beam of surface ions emitted into 4π. It is worth noting that the enormous difference in particle flux for protons originating from the two different sources, i.e., target front and back side, were not observed in 2D-PIC simulations which we performed for comparison. This shows the necessity of taking into account the full three-dimensional geometry, when describing the interaction of the laser with a spherical target. From the above considerations we conclude that we observed protons which were accelerated from the front of the target in a converging shock launched by the impinging laser pulse.

In summary, we report on the experimental observation of strongly directed proton beams emitted from spherical mass-limited targets. When irradiated with an ultrashort, highly intense laser pulse, a converging shock front forms at the front side of the target. Protons accelerated in this shock reach energies well in excess of the values observed in the TNSA regime under identical laser conditions, showing a plateau-shaped spectrum as predicted by Silva *et al.* [16]. Our observations are supported by 3D-PIC simulations with overdense proton plasmas. The radiation pressure model for ion acceleration was extended to a radially dependent intensity profile and successfully implemented to reproduce the shape of the shock front obtained from our PIC simulations. Efficient generation of collimated energetic ion beams from spherical targets is of great interest for the development of laser-driven accelerators. Moreover, the use of high-contrast laser pulses will ultimately result in an almost perfectly converging shock front. Energy deposition of the focused ions will lead to high energy densities with interesting opportunities for fast-ignition concepts and neutron generation.

This work was supported by DFG under Contract No. TR18, DFG cluster of excellence MAP, CICYT Project No. ENE2006-06339 and by the EURATOM/IPP association. A. Henig, D. Kiefer, and S. G. Rykovanov acknowledge financial support from IMPRS-APS, J. Schreiber from DAAD.

*andreas.henig@mpq.mpg.de

[1] S. C. Wilks *et al.*, Phys. Plasmas **8**, 542 (2001).
[2] L. Robson *et al.*, Nature Phys. **3**, 58 (2007).
[3] J. Fuchs *et al.*, Nature Phys. **2**, 48 (2006).
[4] J. Schreiber *et al.*, Phys. Rev. Lett. **97**, 045005 (2006).
[5] M. Roth *et al.*, Plasma Phys. Controlled Fusion **44**, B99 (2002).
[6] J. Schreiber *et al.*, Appl. Phys. B **79**, 1041 (2004).
[7] P. McKenna *et al.*, Phys. Rev. Lett. **98**, 145001 (2007).
[8] J. Limpouch *et al.*, Laser Part. Beams **26**, 225 (2008).
[9] A. J. Kemp and H. Ruhl, Phys. Plasmas **12**, 033105 (2005).
[10] J. Psikal *et al.*, Phys. Plasmas **15**, 053102 (2008).
[11] S. Karsch *et al.*, Phys. Rev. Lett. **91**, 015001 (2003).
[12] S. Busch *et al.*, Appl. Phys. Lett. **82**, 3354 (2003).
[13] R. Ramis, R. Schmalz, and J. Meyer-ter-Vehn, Comput. Phys. Commun. **49**, 475 (1988).
[14] URL http://www.srim.org.
[15] M. Geissler, J. Schreiber, and J. Meyer-ter-Vehn, New J. Phys. **8**, 186 (2006).
[16] L. O. Silva *et al.*, Phys. Rev. Lett. **92**, 015002 (2004).
[17] J. Psikal *et al.*, Czech. J. Phys. **56**, B515 (2006).
[18] S. C. Wilks *et al.*, Phys. Rev. Lett. **69**, 1383 (1992).